Positive Encounters: An Investigative Study on the Effects of Interactions between Cations and Quantum Dots

Erica Q. Chong

A dissertation submitted in partial
fulfillment of the requirements for
the degree of

Doctor of Philosophy
University of Washington
2016

Reading Committee:
Xiaosong Li, Chair
Lutz Maibaum
Brandi Cossairt

Program Authorized to Offer Degree:
Department of Chemistry

University of Washington

Abstract

Positive Encounters: An Investigative Study on the Effects of Interactions between Cations and Quantum Dots

Erica Q. Chong

Chair of the Supervisory Committee:
Professor Xiaosong Li
Department of Chemistry

Semiconductor nanocrystals, also known as quantum dots (QDs), have gained much popularity in recent years not only in the researching community but also in general public. Within researching circles, there are many areas of application that are studies are honing in from the QDs utilization in cellular imaging to light-emitting diodes and beyond. In this particular study, the energy storage characteristics are investigated along with the role that cations may play.

The process of ion diffusion of group I cations (H^+, Li^+, and Na^+) through various anionic, $(MX)_{84}^-$, nanocrystals (with M=Zn, Cd and X=S, Se) were studied. Utilizing the discrete variable representation (DVR) method, the one-dimensional nuclear Schrödinger equation bound solutions for the cations were analyzed. Utilizing these results, further investigation was conducted to determine whether or not the intercalating ions were quantum or classical in nature.

Contents

List of Abbreviations

CB: Conduction band

DFT: Density functional theory

DOS: Density of states

DVR: Discrete variable representation

HOMO: Highest occupied molecular orbital

IDP: Intrinsically disordered protein

MoRF: Molecular recognition feature

PES: Potential energy surface

PQC: Protein quality control

QD: Quantum dot

SCF: Self-consistent field

VB: Valence band

Acknowledgments

The first of my thanks goes to my Lord and Savior, Jesus Christ. Without creating such an intricate universe by which we live, I would not have these unique systems to have studied. Thank you for your love and unending patience. Great is Thy faithfulness. Thank you, also, for putting key people in my life to walk with me, challenge me, and draw me closer to You.

Next, my thanks goes the constants in my life: my family – Dad, Mom, Marie, and Brian. Thank you for your continual love and support. Thank you for the calls to check in on me, the care packages, and most importantly, your prayers. Thank you for being my role models in work, relationships, and faith. I am blessed to have a family so constant in love. Thanks also goes to Auntie Therese and family. Thank you for being my close-by getaway while I've been out here in Seattle.

To the Holcombs, my honorary family, thank you for becoming my support system as I first tested my wings of independence when I had moved out to Mississippi. Thank you for the sanity breaks, not only for most of the weekends of undergrad, but also for the special trips ”home” for various holidays. Thank you for letting me be an honorary Holcomb – a daughter, big sister, granddaughter, and niece.

To my Seattle parents, Ken and Francie, thank you for being so constant these past five years I've lived with y'all. Francie, thank you for being my walking-buddy to school. Ken, thank you for the coffee breaks and letting me be your TV-buddy. Thank you both for being my late-night ride home when I've burnt the midnight oil at work. I've loved all the meals shared, stories swapped, and I am truly blessed to have been able to live with y'all all these years.

To my housemates over the years – Sarah Duffy, Carolyn Valdez, Sophia Sidhu, Laura Dailey, Ruth Moon, Anna Johnson, Carrie Allen, Sara Wong, Renee Gibbs, Ryosuke Akiyama, and Emily Krogstad: I appreciate you all! Thank you for putting up with me when I was stressed, the messes I would make when the papers I would be grading were strewn about the living room, the unsociable side of me when I would need to sequester myself in my room for hours on end to work. I cherish all the heart-to-heart

conversations, dancing and singing, movie nights, card games, midnight tea and coffee breaks, summer kayaking, and all the other small moments shared over the years.

In no preferential order, to Lisa Lee, Daniel Wilson, Rami Foster, Tyler Stevens, Phu Nguyen, Ellen Ashley, Leesa Kurtz, Stephanie Stanley, Katie Weiss, Sean Yeung, and Joshua McDill, thank you for being there celebrating the highs and walking with me in the lows of life. In the phone calls, coffee breaks, meals out, game nights, I am so glad I've had y'all in my life these past six years.

Chapter 1

Introduction

1.1 Motivation

Quantum dots (QDs), which are nanosized semiconductors, were first discovered and studied in the 1980s when they were grown in a glass matrix[1] and in colloidal solutions.[2] One type of QD that is commonly studied today are the II-VI semiconductors which are IIB elements (Zn and Cd) bound to chalcogens (O, S, Se, Te). These crystalline structures have diameters that range from 2-10 nm, though a diameter of 4 nm or greater is more commonly synthesized. A theoretical model of one such QD can be seen in Figure 1.1.

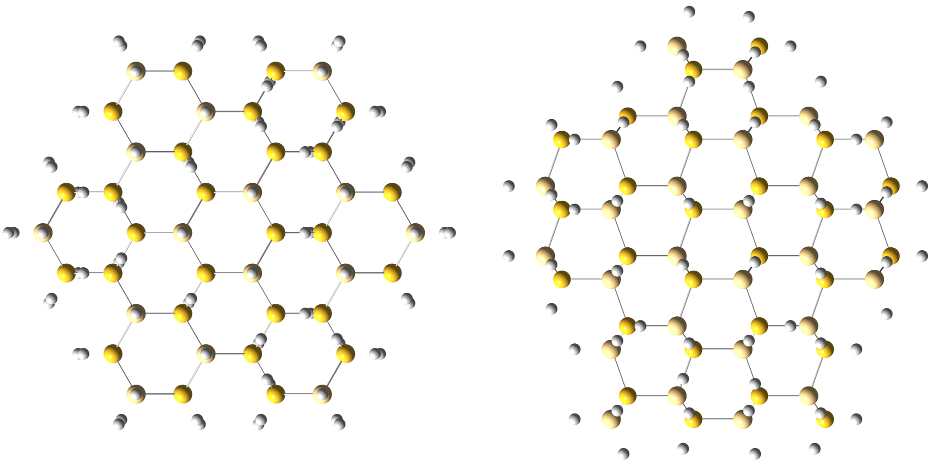

Figure 1.1: Ball and stick representations of $(CdS)_{84}$ which is 2.05Å in diameter. Left panel is through the QD along the C_{3v} axis and right panel is a side profile.

A feature of all semiconductors is the fact that there is a band gap that separates the electron-rich valence band from the conduction band. When an electron is promoted from the bound valence band into the conduction band of the material, there is a positive “hole” that is left behind. The electron in the conduction band and the hole in the valence band can be held together by electrostatic attraction to form an exciton pair. An exciton Bohr radius is the distance between the electron-hole pair.

When the size of a nanocrystal semiconductor is on the same order (or even smaller) than the size of the bulk semiconductor Bohr exciton radius, quantum confinement effect occurs and the continuous ”band” of energies in the valence and conduction bands become discretized energy levels. With this discretization of energy levels, unlike traditional, bulk semiconductors which have a fixed band gap, the band gaps of QDs become size-dependent in a manner similar to the particle-in-a-box model – a decrease in the size of a QD would increase the band gap distance. With the ability to control the size of the QD (and its band gap distance), one can therefore adjust the energy required to excite an electron and conversely, the energy that would be radiated from the QD with an electron-hole recombination. From this, a prominent attraction that arises for the utilization of nanocrystals is the tunability of its electronic and optical properties.[3]

Quantum dots have become materials of interest in the fields of photodetectors,[4] light-emitting diodes,[5], medical imaging,[6] solar cells,[7] among others. One main motivation behind a lot of the research presented in this thesis is the possible implications of utilizing quantum dots as anode materials within rechargeable batteries.

Popular for its high energy density, lack of memory effect (meaning the battery need not be completely discharged before recharging), and low self-discharge, lithium-ion batteries have been prevalently used in today’s modern society. However, one main drawback with these batteries is that its degredation might lead to it lasting only a few years after production. Therefore, manufacturers and researchers are on the look out for novel methods of increasing the efficiency and lifespan of these rechargeable batteries.

ZnO nanowires came under consideration for as a lithium ion battery material since it has a higher theoretical capacity than the more commonly used graphite. However, it was seen that as lithium ions diffused through the nanowires, a ”leapfrog” cracking began to form about 70 nm ahead of the lithiation front. Furthermore within a few charging cycles, the cracking was to the extent that rendered the battery unable to be charged.[8]

It was hypothesized that electrically charged II-VI nanocrystals[9] exert a driving force for charge-compensating cations to diffuse into the QD structure.[10] Since this method is similar to the charging mechanism of lithium-ion batteries, the framework is set up to see that quantum dots are a more favorable battery material than the nanowires due to the fact that its small structure (being smaller than the leapfrog cracking span seen in the nanowire study) would be resistant to cracking in the ion-diffusion process.

1.2 Thesis Trajectory

Outlined below is the flow of this dissertation paper.

In this first chapter, the background of quantum dots and motivation for studying the diffusion process through quantum dots was presented.

In the following chapter, a historical recap for the rise of quantum mechanical background will be given. Also, a brief look at the computational details that are utilized in the calculations for this project are described.

In chapter three, a slight detour down memory lane will be taken to my first solo project. This project had a biology twist as it centered proteins. A specific class of proteins called intrinsically disordered proteins (IDPs) had been found to have the potential to act as quality control systems to work against misfolded proteins which could aggregate and cause diseases. The focus was to study how well one particular IDP, San1 ubiquitin ligase, might bind to various strands of misfolded protein sequences. While the project did not go to full completion, an honorable mention in this thesis was deserved.

Re-entering the world of quantum dots, the dissertation path will conclude upon the findings for the scenario in which a cation is able to diffuse into a reduced quantum dot. A variety of cations and various anionic nanocrystals hosts will be tested so as to lay the groundwork for further investigation to the optimal QD-cation combination that could be used as a battery material.

Chapter 2

Quantum Mechanical Background

2.1 A Brief Recap on the Birth of Modern Quantum Mechanics

Since the 1800s when various dilemmas like blackbody radiation, the photoelectric effect, and the bright line optical spectra were encountered, scientists have been challenged to think in terms beyond that of classical mechanics. This challenge led the way towards quantum mechanics. Quantum mechanics can be defined as the rules of physics in which the intricate workings of matter – such as motion, forces, and energy levels on the atomic and subatomic level can be explained. Building on the previous work of Einstein, Bohr, Planck, and others, in a one-year period – between between 1925 and 1926, modern quantum mechanics was born with the work of three men: Werner Heisenberg, Erwin Schrödinger, and Paul Adrien Maurice Dirac.

Heisenberg, through matrix mechanics, was able to prove that energy states were quantized and time-independent. He is perhaps most notably known for the Heisenberg Uncertainty Principle, which states that the exact location and momentum of a particle cannot simultaneously be known. This can be expressed mathematically as $\delta p \delta x \geq {}^{\hbar}\!/_{2}$. Dirac utilized operator algebra as his main tool to develop theories for modern quantum mechanics which incorporated relativistic effects. Included in his theories were novel concepts such as anti-matter and positrons.

In the time between Heisenberg's first version of quantum mechanics and the works of Dirac, Schrödinger made a breakthrough in the quantum mechanics world. Working off of de Broglie's theory that matter also had wave-like properties, Schrödinger strove to provide a visual approach to the atomic structure. His theorizing resulted in the pivotal Schrödinger time-independent wave equation:

$$\hat{H}\Psi = E\Psi \tag{2.1}$$

in which H is the Hamiltonian or energy operator, E is the energy structure of the system, and Ψ is the wave function. An operator may be regarded as a function, transformation, or map that associates elements of one set to elements from another set. A wave function is a mathematical function used to calculate any physical property of a system. Through the Schrödinger equation, the wave-particle duality of an atomic system can be portrayed.

2.2 Computational Details

Schrödingers equation (Equation 2.1) is pivotal when dealing with quantum mechanics and computational chemistry. When solving this equation for a molecular system, the appropriate form of the Hamiltonian must be incorporated. This molecular Hamiltonian is made up of five energy terms relating to the kinetic (T) and potential (V) aspects of the system. A molecular Hamiltonian can be shown as the following:

$$\hat{H}_{mol} = T_n + T_e + V_{ne} + V_{ee} + V_{nn} \tag{2.2}$$

T_n represents the kinetic energy of the nucleus, T_e is the kinetic energy of the electron, V_{ne} is the electrostatic potential of the nuclear-electron attraction, V_{ee} is the electron-electron repulsion, and V_{nn} is the nuclear repulsion. Due to the complexity in the number of variables, only in the simplest of cases can the Schrödingers equation be solved using the molecular Hamiltonian.

The Born-Oppenheimer or “frozen-nucleus approximation is therefore employed as a means of simplification of the molecular Hamiltonian. While both the nucleus and electrons of a molecule are always in motion, this Born-Oppenheimer approximation states that relative to the kinetic energy of the electron, the nuclei appear to be “frozen.” Therefore, the molecular Hamiltonian is reduced to the following electronic Hamiltonian:

$$\hat{H}_e = T_e + V_{ne} + V_{ee} + C \tag{2.3}$$

since the nucleus appears to be motionless, the kinetic energy of the nucleus, T_n, is reduced to zero and the nuclear repulsion, V_{nn}, remains frozen as a constant.

While this electronic Hamiltonian can be solved for one-electron systems T_e and V_{ne} can be solved on a one-electron basis once there is more than one electron, it is impossible to solve this Hamiltonian exactly for electron movement is correlated and the motion of one affects another, rendering the Hamiltonian inseparable. This Hamiltonian is therefore approximated through numeric methods. This is where computational chemistry comes into effect. Different levels of theory in computational chemistry arise from the way the electron correlation is treated. In this research project, the self-consistent field theory (SCF) and density functional theory (DFT) were employed.

When comparing the theories, the SCF theory (also known as the Hartree-Fock theory) is the most basic. SCF is a combination of both variational theory and perturbation theory since this theory uses both variational calculus and the method of building on the exact known solution of one-electron systems. What SCF does is it ignores individual electron-electron repulsion, and instead treats it as an average, so a single electron would only feel the average of all the other electrons in a system.

Variational theory is used by first choosing a trial wave function that has a variable set of parameters that can be adjusted. The expectation value for the energy is then calculated according to these parameters. The first derivative of the energy is set to equal zero since mathematically, the first derivative of any local maximum or minimum is zero. The parameters are then changed so that this minimum can be produced and then the energy can be found. This approximated energy will always be an upper bound, higher than the exact energy.

Perturbation theory does not use parameters nor a trial wave function. It approximates the true Hamiltonian to be similar to another Hamiltonian in which the wave function is known. Therefore, the total of a system is composed of two parts – the unperturbed Hamiltonian and the perturbation which causes a slight alteration into the unperturbed Hamiltonian. Perturbation theory involves Taylor series expansions of the energy and the wave function that are truncated after a chosen number of terms. The order of the perturbation correction increases based on the number of terms of the Taylor series utilized in the correction.

Within the SCF theory, molecular orbitals are the group of eigenfunctions of a one-electron operator and the variational parameters are the coefficients for the atomic orbitals that make up the molecular orbitals. With these molecular orbitals, some will be occupied, others will either be unoccupied or virtual. SCF theory seeks to minimize the energy since the lower the energy, the more accurate the calculation. However, since SCF theory does not consider electron correlation, the difference between the upper bound and the actual energy of the system would be the electron-electron correlated effects and the relativistic effects which include spin-coupling effects.

For DFT, energy is computed through the use of functionals. The electronic energy is a function of the electron density which is a function of coordinates in real space. The functionals partition electronic energy into components which are computed separately: kinetic energy, Coulombic electron-electron repulsion, electron-nuclear interaction, and exchange correlation term.

Since an exact energy functional is unknown, various methods are utilized to approximate functionals. The simplest of functionals used is the local density approximation (LDA), in which the assumption is made that energy depends locally on density similarly to a uniform electron gas. Local spin density approximation (LSDA) is a generalization of LDA that includes spin. The generalized gradient approximation (GGA) takes into account a gradient density instead of the uniform density that LDA assumes.

Another variety of functionals are hybrid functionals which mix some exact exchange with a GGA. One of the most popular hybrid functional is B3LYP which uses a combination of a three-parameter hybrid GGA exchange functional developed by Becke (B3) with a GGA correlation function developed by Lee, Yang, and Parr (LYP) that not only approximates the full correlation energy but also corrects the error caused by self-interactions in single-electron systems. While B3LYP has empirical parameters set by experts, on the flip side, there exists non-empirical functionals which use only general rules of quantum mechanics and spatial limiting conditions to determine parameters in general forms. For the QD calculations run in this thesis, the DFT hybrid functional PBE1PBE (Perdew-Burke-Ernzerhof) which uses a mixture of 25% HF exchange and 75% electron-correlation with LANL2DZ pseudo-potential basis set were utilized.

Chapter 3

The search for interaction partners of the intrinsically disordered protein, San1 ubiquitin ligase

3.1 Background and Introduction

Intrinsically disordered proteins (IDPs) are a class of proteins that lack well-defined structures[11,12]. Prevalent amongst eukaryotic proteins, IDPs are found to be biologically functional and can interact with other proteins[13]. This brings forth the question of how such interactions occur since classically protein-protein interactions have been studied within the context of well-defined three-dimensional structures.

When proteins become misfolded which can result from a range of scenarios from chemical or physical hazards to synthesis errors there is a tendency to have a build-up of toxic aggregation-prone sites. This protein aggregation has been found to be a common link between neurodegenerative disorders such as Huntingtons diseases, Parkinsons disease, Alzheimers disease, amyotrophic lateral sclerosis, and prion diseases[14].

Within the cell are protein quality control (PQC) systems to deal with aberrant proteins. An example of a PQC system is represented by the protein chaperones that bind to the misfolded proteins to either induce refolding for some-times when a misfolded protein binds with a partner, it will undergo a disorder-to-order transition or to sequester the persistently misfolded proteins. If a cell cannot repair an aberrant protein, it will seek to destroy that protein to prevent toxic aggregation and maintain order within the cell. One such agent of degradation is the San1 ubiquitin ligase, which, interestingly, is an IDP[15]. It has been studied that nestled within regions of disorder of IDPs are small segments (around twenty residues) called molecular recognition features (MoRFs)[16]. It is fortuitous that San1 is an intrinsically disordered protein because as such, it has a flexible structure[13] that is able to adapt to different orientations to bind to a misfolded protein (see Figure 3.1)

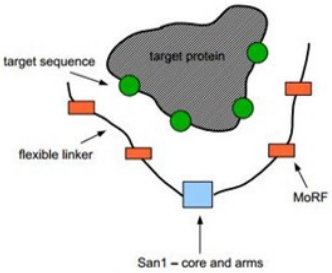

Figure 3.1: A schematic of MoRF-Target interaction

The hypothesis guiding this research study is that there are specific interaction partners for proteins. These interaction partners are not defined by structure, but by perhaps a specific sequence. In the case of San1, research has found that MoRFs within this ubiquitin ligase can identify and target exposed regions of hydrophobicity (at least five contiguous hydrophobic residues) in other proteins[17]. Since San1 has been found to be an agent of nuclear degradation of misfolded proteins[15], it would be greatly beneficial to be able to identify the interaction partners that are responsible for the toxic aggregation. If this objective is achieved, then San1 can potentially be used strategically as line of defense against certain diseases such as cancer, neurodegeneration, cardiovascular disease, and type II diabetes[18].

3.2 Method

Peptide sequences for nine MoRFs and twenty-eight Targets were provided by the Gardner research group. Initial molecular structures of these sequences were then modeled using UCSF Chimera software[19]. All subsequent calculations were performed with the development version of the Gaussian suite of programs[20]. Each MoRF and Target was fully optimized using the Amber force field of molecular mechanics. Frequency calculations were then performed using a semi-empirical PM6 method to gain the zero-point energy correction to use as the vibrational energy of the system associated with initial random Cartesian velocities for the atoms of a MoRF or Target. To maintain uniformity, each MoRF and Target was rotated so that the principal axis was aligned with the z-axis.

When setting up the molecular dynamics trajectories, each MoRF-Target combination was translated so that the center of mass of each would initially be 20 Å apart a distance at which there would be no or very small interaction in the ±x and ±y directions to provide four different starting representations for each combination. Each trajectory, given an initial kick of velocity (1×10^{13} Bohr/sec) to propel the MoRF and the Target towards each other, ran for 20 picoseconds with 0.5-femtosecond time steps. A simulated annealing process to remove this extra translational energy was implemented between the 2-picosecond and 3-picosecond time frame. Visualization of the results was done using Molden software[21].

3.3 Results and Discussion

Preliminary results were acquired for MoRF-Target combination trajectories of MoRF6 with Targets 20, 21, 22, 23, 24, and 25 (See Table 3.1 for a listing of sequences). Data analysis of these trajectories began at the 3-picosecond marker after the completion of the simulated annealing process of the initial kick of energy into the system. The total energy conservation is maintained to be less than 0.5 kcal/mol.

It was stated that the goal of this project was to discover interaction partners of the intrinsically disordered protein, San1. Experimentally, dynamical interaction is studied by measuring the free energy in the system. Computationally, such systems are typically represented by a canonical (NVT) or a NPT ensemble to calculate the Helmholtz, $A = UTS$, or Gibbs, $G = HTS$, free energy. Since the current study is held in a microcanonical ensemble, a longer route to calculate the free energy would have to be used. First the microstates, Ω(NVE), would have to be counted, then the entropy, $S(E) = kln\Omega(E)$, would need to be calculated and from there thermodynamic properties can be gathered. The preliminary analysis of the interaction between San1 MoRFs and various targets was conducted by a more qualitative nature through comparing the relative interaction energies of each ensemble.

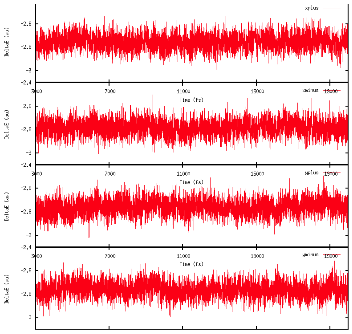

Figure 3.2: Summary of four trajectories of MoRF6-Target24

It could be seen that the energy of each M6-Target combination oscillated about a certain point of energy (see Figure 3.2 for an example). This was encouraging to see for it supported that a microcanonical ensemble had been achieved. An average energy was taken from each combination ensemble. This average was not taken under the assumption that the system is ergodic (which would imply that one trajectory would be equal to an ensemble average of many trajectories), but rather was taken as an attempt to extrapolate a pattern. When looking at Figure 3.2, it can be seen that though a MoRF and Target come together from four different orientations, the energy fluctuates each time around basically the same energy. These fluctuations encode interactions between MoRF6 and each Target. However, the degree of interaction was still to be determined. When visual-izing the trajectories with Molden, the MoRF and Target are seen to equilibrate and have an affinity for each other. With the combinations tested, there has yet to be seen a trajectory in which the MoRF does not interact at all with the Target. In order to gain the interaction energy of a system that was not affected by its individual components, an initial attempt was to incorporate the following equation:

$$\Delta E = E_{system} - E_{ZPE\ MoRF} - E_{ZPE\ Target}$$

where ΔE represents a relative interaction energy, E_{system} is the potential energy of the system, and the last two terms are the zero-point energies of the MoRF and Target acquired from the semi-empirical PM6 calculation. Though this equation resulted in unrealistic results (see Table 3.2 for values), the results can be used to gain a preliminary unbiased comparison between the interaction between a specific MoRF and various Targets.

It can be seen that of the MoRF6-Target combinations completed thus far, MoRF6 shows the highest likelihood of binding with Target21 since that pairing had the lowest ΔE. The next best choice for a potential interaction partner is Target24. As the full range of twenty-eight Targets are tested with each MoRF, based on the calculated ΔE, a ranking of best-to-least interaction probability will be given back to the Gardner research group to compare with their experimental data. Matching data will be the desired evidence that our current method is running on the correct path.

Proposed future work includes the introduction of solvents into the system. Since the current trajectories were simulated in vacuum-phase, all the peptides were adjusted to be neutral. If solvation (i.e. a water box) were to be used, then the MoRF and Target compounds can better mirror their actual environment. Effects of hydrophobicity can also be able to be investigated.

MoRF6 (M6)	GSSFLENISRLTGHFT
Target20 (T20)	TGGPSLSQKEGRVGVM
Target21 (T21)	RDTLSQAQDTMLRLGL
Target22 (T22)	RFSMMEVTGWSVRFLG
Target23 (T23)	SRKGWWLLCWGGQALF
Target24 (T24)	TEEALMRLSRCAETSR
Target25 (T25)	SEEADMDRRSSYVCAN

Table 3.1: Listing of sequences of MoRF6 and various Targets

Combination	ΔE (a.u.)	ΔE (kcal/mol)
M6-T20	-2.148	-1347.7
M6-T21	-2.770	-1737.9
M6-T22	-2.467	-1547.9
M6-T23	-2.092	-1312.5
M6-T24	-2.766	-1735.4
M6-T25	-2.359	-1480.1

Table 3.2: Summary of calculated averages of adjusted potential energy and ΔE

Chapter 4

Classical or Quantum? A Computational Study of Small Ion Diffusion in II-VI Semiconductor Quantum Dots

4.1 Abstract

Ion diffusion in semiconductor nanocrystals, or quantum dots (QDs), has gained recognition in recent years as a crucial process for advancing both energy storage and, more generally, the post-synthetic *p*-type doping chemistry of these materials. In this report, we present first an energetic analysis of group I cation (H^+, Li^+, and Na^+) diffusion in $(MX)_{84}^-$ QDs, with M=Zn, Cd and X=S, Se. The bound solutions to the corresponding one-dimensional nuclear Schrödinger equation were solved for these systems, relying on the discrete variable representation method. From this vantage, the quantum nature of the intercalating ion can be revealed. Evidence for the importance of including quantum effects in the treatment of these diffusion processes is presented, both with the density of energy eigenstates of the intercalating ion and from a comparison of the uncertainty in the position of the intercalating ion to the lattice spacings of its host material. Results suggest that the use of classical mechanics for simulations of the ion diffusion processes in these and other related materials can be a questionable practice for the smallest group I cations. Trends devised herein can be useful to help guide the development of new experimental approaches to post-synthetic doping of semiconductor nanocrystals, and in designing electrode materials for next generation electrochemical energy storage devices.

4.2 Introduction

The processes by which small cations intercalate and are eventually incorporated into the lattices of crystalline materials have become an active area of investigation in condensed matter physics and fundamental materials sciences.[22–30] Materials that exhibit ionic diffusivity present a diverse range of technological applications, including energy storage,[31,32] chemical sensing,[33] and emerging spintronic[34] and optoelectronic[35,36] devices.

Materials that allow the transmission of ions from one face of a crystalline solid to another have been known for some time now, and have found uses as solid electrolytes and electrode separators in solid-state fuel cells and batteries. Ionic migration in many of these materials is mediated by lattice vacancies, through which the conducted ions can be effectively shuttled. This is an example of a slow, "substitutional diffusion" process.[22] However, a more expedient mechanism of ionic transport through crystalline materials exhibiting interstitial migration channels is also possible.[37–40] Various binary semiconductors (TiO_2, ZnO, CdS to name a few) contain extended, linear interstitial diffusion pathways that permit the relatively unhindered diffusion of small ions through the interior corridors of their crystalline lattice (as seen in Figure 4.1). The uptake of charge balancing cations by such semiconductor materials upon electrochemical reduction was investigated via electrochemical quartz crystal microbalance studies, which demonstrated a one-to-one correspondence between the extent of reduction of the II-VI semiconductors and their mass gain.[41] It has also been shown that smaller counter-ions enable the semiconductor to be more reduced than larger ones.[42,28] The nonlinear relationship between the counter-ion size and the extent of electronic charging achieved suggests that above a certain size threshold, large counter-ions must reside strictly at the crystal surface, while smaller ions may intercalate to homogeneously fill the interstitial sites intrinsic to certain crystal lattices.

Recent theoretical work on the II-VI semiconductor ion diffusivity have shown that interstitial diffusion and ion substitution processes are correlated, and suggest that the delicate balance of these two processes can affect the electronic and structural properties of the resulting semiconductors.[43] Beyond varying the choice of shallow-donor intercalant to be employed in the diffusion doping procedure, the composition of binary semiconductors can also affect the doping chemistry. Changes in the composition of the binary semiconductor can modulate the electronic and geometric aspects of the system, affecting the internal barriers to diffusion and, therefore, the trapping kinetics.[44] For example, sulfide-based semiconductors may be better candidates for proton diffusion doping than oxides, because the S-H bond is usually less strong than O-H, leading to lower interaction potential between the intercalant and host lattice. Likewise, Cd-based materials could be better suited for diffusion doping technique than Zn, because they have comparable electronegativities but give rise to more spacious intercalation channels in the crystal lattice.

Future alkali metal-based batteries will benefit from nanostructured electrode materials, since such morphologies offer a higher theoretical capacity and an improved rate of diffusion of charged ions relative to the bulk materials.[45] Improving the performances of these materials for energy storage (batteries) and the insertion (intercalation) and extraction (de-intercalation) of lithium ions from the electrode materials has become the object of several experimental and computational studies to optimize the factors that presently limit charge capacity and power.[32,31] The ion diffusion process in semiconductor nanocrystals has implications reaching beyond its obvious role in energy storage technologies. By exploiting ion diffusion and lattice substitution processes in II-VI semiconductor materials, a post-synthetic doping procedure for nanostructured semiconductors has been developed.[46–48] This approach represents a promising route for overcoming the challenges of reproducible *p*-type II-VI semiconductor (e.g. ZnO) preparation via the partial substitution of Zn^{2+} for group I elements such as H^+, Li^+, and Na^+.[49] A more detailed understanding of the the condensed-phase diffusion dynamics can give crucial insight to help guide new synthetic doping methodology development efforts.

In this study we investigate the energetic barriers for one-dimensional interstitial diffusion within several metal chalcogenide semiconductors approaching the nanosize. A systematic investigation of the group I elements (H^+, Li^+, and Na^+) diffusion in $(MX)_{84}^-$ quantum dots (QDs, with M=Zn, Cd and X=S, Se) is presented.

First principle methods, exploiting the reliability of density functional theory (DFT) for this class of system, combined with an explicit numerical solution of the nuclear Schrödinger equation, were used. This gives an effective strategy for resolving the discrete energy spectrum via quantum treatment of light intercalants that can account for the anharmonicity of the potential energy surface along the diffusion channels, providing a more accurate description of the interstitial diffusion of positively charged ions into several nanosized semiconductor QDs.

It's nowadays well established that excitonic states in semiconductor nanocrystals below a critical size (less than the Bohr radii of excitons) exhibit a marked increase in the kinetic energy of photo-generated charge carriers relative to analogous states in bulk-scale materials.[50–52] In this work, we consider how a light atom placed into the linear diffusion channels of wurtzite-phase II-VI semiconductor nanocrystals may have its energy spectrum modulated by the small size of the system. That is, we aim to elucidate under what intercalating ion sizes and nanocrystal compositions may these ‘quantum confinement’ effects manifest in the energy spectrum of linearly-diffusing light ionic species in the nanocrystals. Finally, a careful analysis of the importance of quantum effects in describing the time evolution of the light intercalating particles within diffusion channels in the II-VI semiconductors is presented, and effects of dynamical disorder such as lattice vibrations on the ion diffusion dynamics are considered.

4.3 Methodology

4.3.1 Electronic Structure Calculations

All electronic structures calculations were performed using the development version of the Gaussian program.[53] Nearly spherical wurtzite phase $(MX)_{84}^{-}$ quantum dots (with M=Zn, Cd and X=S, Se) exhibiting C_{3v} symmetry were built (diameter: ZnS ∼1.90, ZnSe ∼1.98, CdS ∼2.06, and CdSe ∼2.14 nm, see Figure 4.1) according to the previously published scheme[54,55] and using the lattice parameters from the American Crystal Structure Database.[56] The dangling bonds on the surface of the nanocrystals were passivated with pseudohydrogen atoms having modified nuclear charges of 0.5 and 1.5 to terminate surface X^{2-} and M^{2+} ions, respectively.[54,55] The charge of each QD was set to -1 to simulate the system being reduced. The PBE0 hybrid DFT functional was used[57–59] along with the Los Alamos double-ζ pseudocore potential and the associated valence double zeta basis (LANL2DZ) for the lattice,[60–62] and the all-electron, cc-pVDZ[63] Dunning-type basis for the intercalant. This methodology has already shown very promising results in our lab for the theoretical characterization of diluted magnetic semi-conductor, i.e doped zinc-oxide QDs.[55,64–69]

Rigid scans were performed with each combination of the singly-reduced QD and ion of choice (H^+, Li^+, Na^+). Each ion was passed through the QD along the C_{3v} -axis shown as the dashed line in Figure 4.1, starting from a configuration in which the ion and the QD are mostly non interacting, ensuring us a consistent reference energy, and using a fixed 0.3 Å step size resolution. All of the studied systems were modeled in the gas-phase, neglecting the free energy contributions due to the ion/surface/QD solvation. This approximation, along with the surface passivation by way of the pseudohydrogen scheme, mostly affects the potential barrier for entering the diffusion channel, and the current study nonetheless exposes factors influencing the interstitial doping mechanism in QDs, including insights into the relationship between the need for quantum effects to describe the motions of light nuclei and the composition of the QDs. The resulting one-dimensional potential energy surfaces (1D-PES) were used as the potential for the corresponding one-dimensional nuclear Schrödinger equation. Geometry optimization and

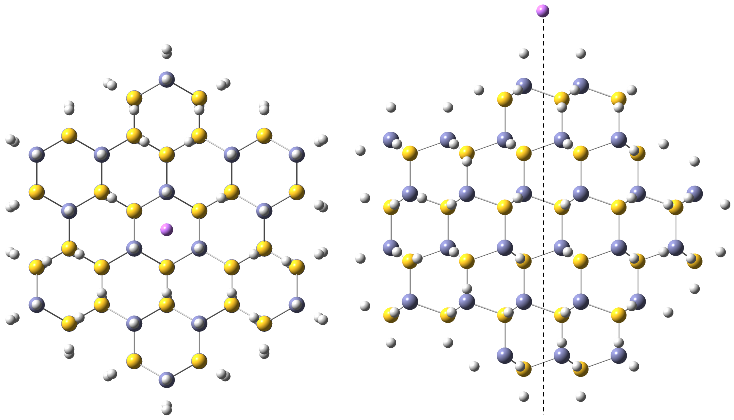

Figure 4.1: Small cation intercalation channel in a II-VI QD (ball and stick model), with diffusing cation in magenta, lattice anion in yellow, lattice cation in blue, and hydrogen in white. Top-down (left panel, with the C_{3v} axis perpendicular to the plane of the page) and profile view (right panel, with the pseudo C_{3v} axis as dashed line) are represented.

harmonic frequency analyses have been also performed on a smaller size $(CdSe)_{33}$ QD still exhibiting C_{3v} symmetry (diameter ~1.36 nm) in order to gauge the lattice relaxation and vibrations effects on the potential.

4.3.2 Nuclear Wave Function Calculations

In order to introduce the anharmonicity and the intrinsic delocalized nature of nuclei, especially relevant for the light nuclei such as hydrogen and lithium, the solution of the nuclear Schrödinger equation over a suitable *ab-initio* PES is required:

$$\hat{H}\Psi_{nuc} = [\hat{T}_{nuc} + U(\mathbf{R})]\Psi_{nuc} = E\Psi_{nuc} \tag{4.1}$$

In Equation 4.1, $U(\mathbf{R})$ is the *ab initio* electronic potential, obtained within the Born-Oppenheimer approximation from electronic structure calculations. In principle, $\mathbf{R}$ is a vector of $3N-6$ components (where N is the number of atoms of the system), describing the nuclear geometry arrangement. In practice, because the large number of components, we chose the 1D-PES obtained from the energetic rigid (without allowing any relaxation) scan along the interstitial diffusion path, obtaining in this way a one-dimensional potential corresponding to diffusion along C_{3v} axis for each ion/QD combination.

To solve the one-dimensional nuclear Schrödinger equation (Equation 4.1), the discrete variable representation (DVR) was used.[70–73] This method has already been successfully applied in several chemical studies.[74–77] The energy eigenstates for small intercalated ions along the C_{3v} axis of the quantum dot were resolved within the DVR. Some questions naturally arise as to the proper description of the electronic potential when treating the nuclear degrees of freedom non-classically. In order to account for the spatial extent of the nuclei in the electronic structure, electron-nuclear attraction terms in the electronic Hamiltonian (and nuclear-nuclear repulsion terms in the full molecular Hamiltonian) should no longer depend parametrically, but rather continuously on the nuclear positions, drastically increasing the expense of resolving the nuclear electrostatic interactions. Here, we approximate the potential experienced by the quantum "fuzzy" nucleus by the potential of classical nuclei diffusing along the C_{3v} axis of a rigid (i.e. fixed nuclear positions) nanocrystal. Asymmetry observed in the potential is a result of the truncation of the lattice and the intrinsic polarity of the II-VI semiconductors in the wurtzite phase. A fine grid comprised of 500 Gauss-Hermite quadrature points was employed in the DVR. The one-dimensional potential energy surface was collected with 0.3 Å resolution, and interpolated by cubic splines. Analytical expression for the matrix elements of the kinetic energy operator in the pseudo-spectral basis were utilized, along with the approximation that the potential operator is diagonal in the basis of spatially-localized, pseudo-spectral functions. This latter approximation is naturally equivalent to the situation in which the Hamiltonian is formed in the spectral basis, and the matrix elements of the potential operator calculated via a numerical quadrature with the same number of quadrature points as utilized in the DVR. The potential outside of the nanocrystal is fixed at the value of the potential at the crystal's boundaries (i.e. at the maximum values at the edges of the PES scans in Figure 4.2). In this way, the low-energy region of the Hamiltonian's spectrum is restricted to the bound states where the cation is contained inside the nanocrystal (that is, scattering state solutions are avoided).

4.4 Results and Discussion

4.4.1 Energetic Analysis

In Figure 4.2, the energetic scans are grouped together to show the potential energy surfaces (PES) of H^+, Li^+, and Na^+ ions intercalating through each particular reduced QD. Table 4.1 lists the average activation barriers of diffusion (forward and backward). Figure 4.3 compares the interstitial barrier heights of diffusion PES for different cations as a function of II-VI QD lattice parameters. A general trend can be seen that the interstitial diffusion barriers increase with the decrease in the QD lattice parameter. Internal intercalation barriers are also shown to increase with the incoming dopant cation's size. H^+, as the smallest cation, is the least sensitive to the nature of the host structures with the lowest barriers, and Na^+, as the largest cation, is the dopant that is most influenced by the host QD structure

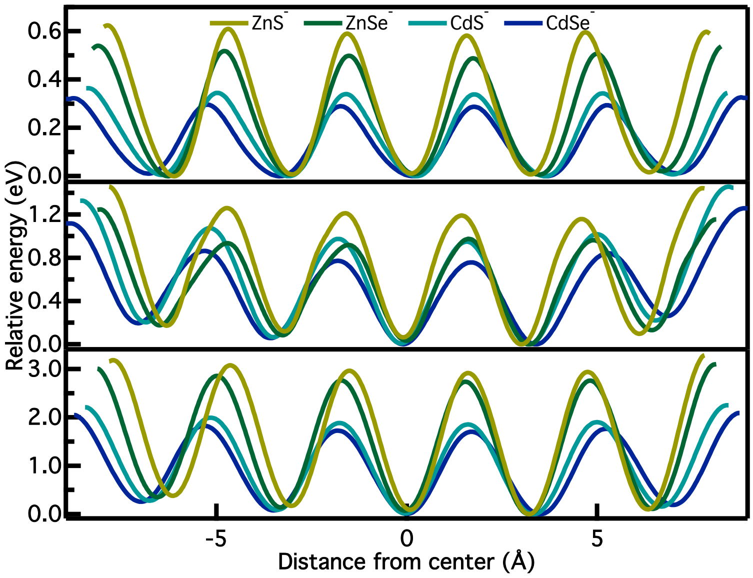

Figure 4.2: PBE0/LANL2DZ rigid 1D-PES for the group I analyzed cations (H^+, Li^+, and Na^+, top, middle, and bottom panel, respectively) diffusing along the C_{3v} axis of QDs (see color legend in the upper panel).

with largest barriers to overcome as it intercalates through the QD.

	H^+ Intercalation (eV)^a	Li^+ Intercalation (eV)^a	Na^+ Intercalation (eV)^a
ZnS	0.579	1.109	2.808
ZnSe	0.485	0.867	2.644
CdS	0.335	0.922	1.809
CdSe	0.286	0.714	1.660

Table 4.1: PBE0/LANL2DZ stationary point energy values (eV) of the average activation barriers for the group I analyzed cations (H^+, Li^+, and Na^+, from left to right) as each diffuses through the QD along the C_{3v} axis of the $(MX)_{84}^-$ QDs (top to down). ^{a} Energies are given relative to the deepest well in each QD 1D-PES.

Lithium diffusion barriers are the result of the two competitive effects of its size and redox potential. Lithium and sodium are most likely oxidized inside the QD compared with hydrogen, meaning that they interact in a more ionic way with the lattice. Therefore the electrostatic interactions with the host cations and anions play an important role in the diffusion process for these two ions. On the other hand, the oxidized sodium is ~30% larger ionic radius than does lithium, meaning that the steric interactions dominate sodium's diffusion characteristics. Of the two competing factors of steric vs. electrostatic interactions, it is understandable that steric interactions decrease as function of the lattice parameter since larger lattice parameters give a wider channel through with the ion can diffuse. However, the ionic character of the QD, which affects its electrostatic interaction with diffusing ions, is not a function

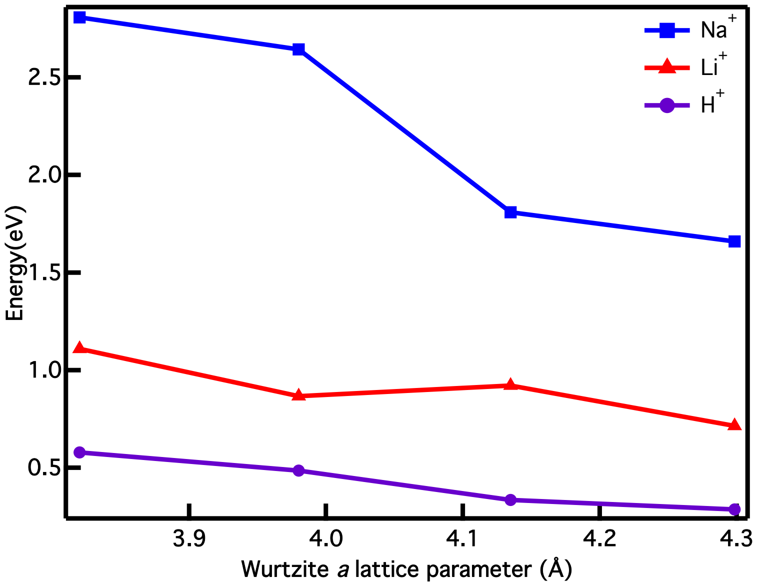

Figure 4.3: PBE0/LANL2DZ average activation energy barriers (eV) for the interstitial diffusion of group I cations (H^+ purple circle, Li^+ red triangle, Na^+ blue square) within QDs as a function of the hosting crystallographic wurtzite lattice parameter, a (ZnS=3.82Å, ZnSe=3.82Å, CdS=4.13Å, and CdSe=4.30Å).

of the lattice parameter (i.e. CdS has a higher ionic character than ZnSe[78,79]). Lithium, while it has larger ionic interactions than hydrogen, is still small enough for its diffusion to not be entirely ruled by the steric interactions that dominate sodium's interaction with the dot. The balance of these two competitive effects can explain lithium's non-linear trend of the activation barrier as a function of the dot size.

H^+ diffusion PES in CdSe QD has the lowest activation barrier and Na^+ has the highest when it diffuses through ZnS QD. H^+ has diffusion barriers that range from ~0.3 to ~0.6 eV (~7 to 14 kcal/mol). For reactions associated with such low barriers, a quantum treatment of nuclei should be taken into account. A more accurate energetic analysis utilizing DVR is presented in the next section.

4.4.2 Quantum Nuclear States in II-VI QDs

Figure 4.4 shows the computed probability distributions and energy levels of lowest several quantum states inside the central well of PES that correspond to a H^+ in QD. DVR analyses of other cations inside II-VI QDs are presented at the end of this chapter. As shown in Figure 4.4, the lowest quantum states are localized inside the central well, and their wave functions quickly decay in the classically forbidden region before tunneling to adjacent wells. As the energy level increases, the delocalized nature of H^+ becomes more significant and the wave function has higher probabilities to tunnel into adjacent wells.

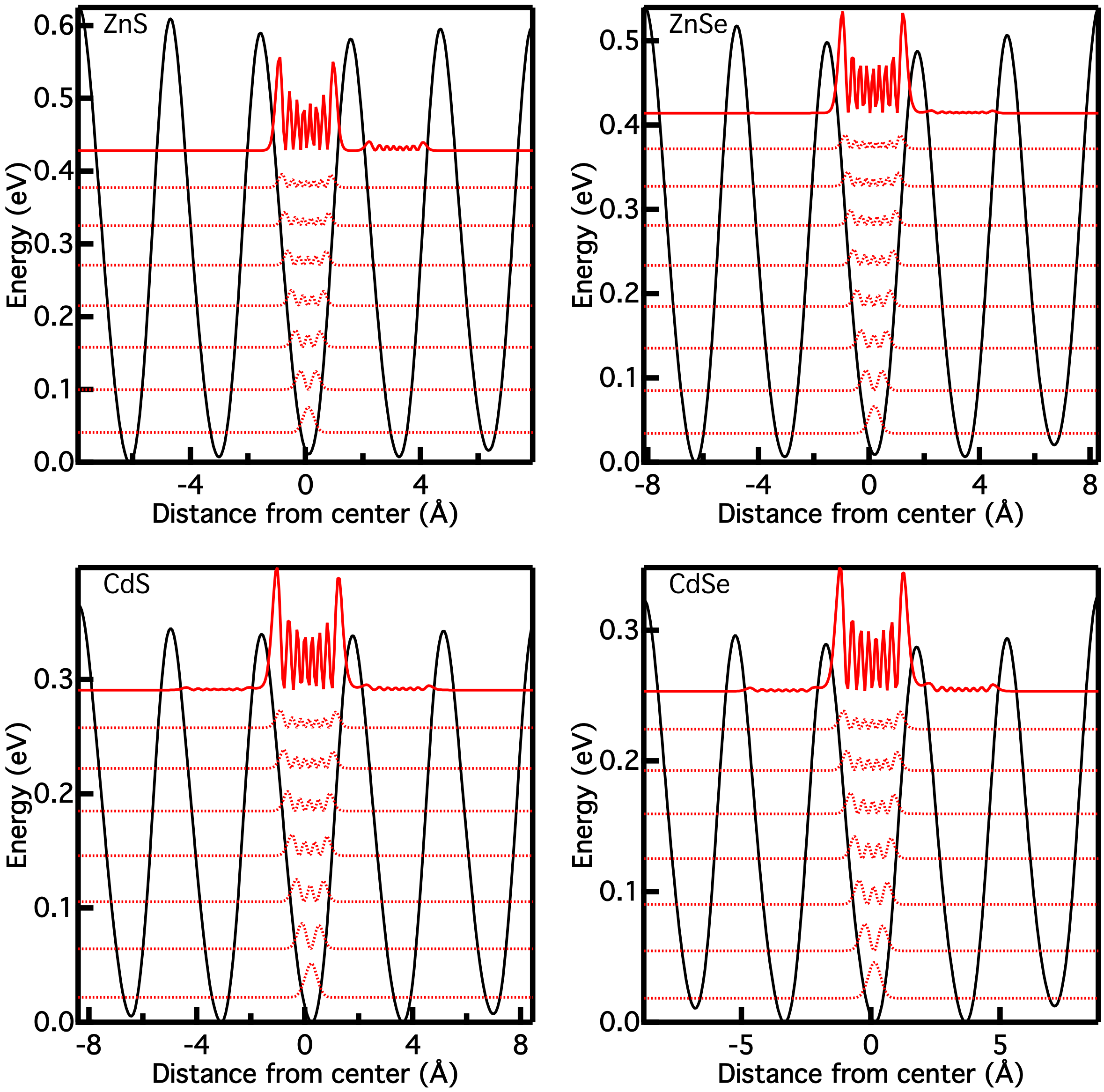

Figure 4.4: Normalized $|\Psi^i_{DVR}|^2$ DVR probability distribution functions (dotted red lines, solid red line represents $|\Psi^i_{DVR}|^2 \times 2$) for hydrogen cation in the analyzed reduced QDs. We reported only the ones localized in the central well up to the first diffused state, without showing the corresponding nearly degenerate solutions (localized in the other wells), plotted so that the corresponding base line matches the associated eigenvalue (relative to the 1D-PES, black line). The probability distributions are calculated as the squared values of the corresponding normalized DVR wave functions.

One outstanding question is whether small cations intercalating in II-VI semiconductor nanocrystals behave predominantly classically or if quantum correction is important for capturing the correct physics for these systems. The quantum/classical question can be approached from the vantage of the density of states (DOS) relative to the thermal energy, $k_B T$. Figure 4.5 shows the DOS plots using the energy levels computed with the DVR technique, demonstrating the trend for the energy spectrum discreteness (relative to k_BT at 300K) for the different intercalating ions and materials. Hydrogen, the smallest and the lightest ion considered, exhibits a spacing between energy eigenstates that is on the order of the thermal energy for both of the zinc-based quantum dots. As the crystalline material is varied from larger to smaller lattice constants, the splittings between energy eigenstates grow, indicating an analogous effect to the excitonic quantum confinement. As the internal barriers of the dot are made higher and the curvature of the PES near minima is sharpened, the low energy eigenstates become more spatially localized, indicating more particle-like (and less wave-like) character.

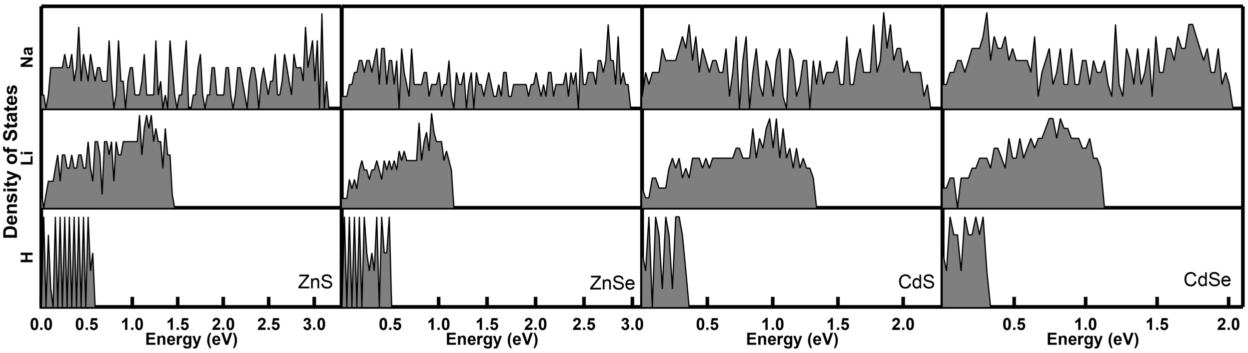

Figure 4.5: Density of energy eigenstates for the various intercalating ions and II-VI semiconductors. Bins in the DOS plots are separated by k_bT at 300K to demonstrate the quantum confinement effects (larger spacing between levels) which are more pronounced for the proton (lower panels) than the other two ions (middle and upper panels).

Another route to discern between these two situations is to compare the typical interaction lengths to the uncertainty in the position of the species of interest. For the current study, the characteristic length-scale for the ion-lattice interactions is given by the distance between adjacent potential minima/maxima along the ion diffusion coordinate. The standard deviation in the diffusing ion's position, $\sigma_R = \sqrt{\langle R^2 \rangle - \langle R \rangle^2}$, was evaluated directly for each energy eigenstate. The thermal averages for these position uncertainties, $\langle \sigma_R \rangle$, (where the brackets indicate a trace over the phase space rather than an expectation value) are evaluated according to Equation 4.2.

$$\langle \sigma_R \rangle = Z^{-1} \sum_i e^{-E_i/k_BT} \sigma_R^i \tag{4.2}$$

where E_i and ψ_i are the i^{th} eigenvalue and eigenfunction of the total Hamiltonian, $Z = \sum_i e^{-E_i/k_bT}$. The position uncertainties for the different intercalating ions and binary semiconductors are given in Table 4.2. Since inter-particles spacings are small in the condensed phase, an exceptionally small uncertainty in the particle's position would be needed in order for quantum corrections to be negligible. The ratio (τ) of the standard deviation of the intercalating species' position to the distance between the particle's mean position and the nearest maximum in the potential along the diffusion coordinate

	$\langle \sigma_R \rangle_{NVT}$ (H^+)	$\langle \sigma_R \rangle_{NVT}$ (Li^+)	$\langle \sigma_R \rangle_{NVT}$ (Na^+)
ZnS	0.1777	0.0792	0.0461
ZnSe	0.1881	0.0824	0.0472
CdS	0.2006	0.0832	0.0497
CdSe	0.2107	0.0862	0.0507

Table 4.2: Thermally-averaged standard deviations of the position (units of Å) calculated for the selected intercalating ions and $(MX)_{84}^-$ semiconductor nanocrystals

	τ_{H^+}	τ_{Li^+}	τ_{Na^+}
ZnS	12.8%	6.47%	4.34%
ZnSe	13.6%	7.18%	4.47%
CdS	15.2%	7.17%	5.16%
CdSe	16.5%	7.69%	5.37%

Table 4.3: Ratios (τ, unitless) of the standard deviation of the position to the distance between adjacent potential minima and maxima along the diffusion coordinate, calculated for the selected intercalating ions and $(MX)_{84}^-$ semiconductor nanocrystals. Higher ratios are indicative of more wave-like character for the intercalating species.

(approximately one fourth the wurtzite lattice parameter, c) are collected in Table 4.3. Captured in these results are the competitive effects of modulating the average barrier heights and width of classically forbidden regions separating adjacent wells as the lattice parameters and ion sizes vary across the different semiconductors and intercalants. This ratio can be a good measurement of the importance of quantum effects of intercalating ions on the diffusion dynamics. For example, a ratio of unity suggests that the wave function of the ion must be delocalized among adjacent interstitial sites, whereas $\tau << 1$ is associated with quantum nuclei localized in a single cavity. Indeed the lowest energy eigenstates delocalized across multiple wells in the PES occur, on average, at $tau = 75\%$ for the proton (see Figure 4.4 for an example of delocalized energy eigenstate). The thermally-averaged standard deviations of the intercalating species' position are observed to be on a similar order of magnitude as the characteristic interaction length scales of the system, yielding τ approaching the threshold for delocalization for the lightest ions studied. It follows then that for the case of H^+ (and to a lesser extent Li^+) intercalation, the intercalation dynamics can be substantially modified by the quantum effects. The τ value for Na^+ in all QDs considered here is $< 6\%$, suggesting a mostly classical behavior.

The intercalants show different trends in the sensitivity of their τ values to the lattice spacing of the different semiconductors. While the delocalization of the intercalant increases with increasing lattice spacing, the three cations show different rates of change in τ with respect to the lattice parameters. This is a consequence of two competing factors. The increasing lattice size leads to lower diffusion barriers, but also to an increasing width of the confining potential and classically forbidden region, and as a result a lesser quantum confinement effect and smaller probability to tunnel through the barrier. At the same time, the energy spacing decreases leading to a more continuous manifold of (bound) energy eigenstates and more classical behavior. In the case of H^+, the quantum diffusion effect arising from the lower diffusion barriers outpaces the suppressing effect, while the quantum effects are damped for Li^+ and Na^+ by the wider classically forbidden regions they experience at lower, thermally-relevant energies.

4.4.3 Effects of Lattice Relaxation and Vibration on Quantum Diffusion

Potential energy surfaces obtained from rigid scans do not take into account any changes that might occur within the framework of the lattice structure of the nanoparticle, such as structural relaxation and lattice vibrations, which can significantly alter the ion diffusion PES. In the previous section, it has been seen that the diffusing Na^+ acts predominantly as a classical particle, while H^+ (and to a small extent Li^+) begins to show quantum behavior. The question is now presented, what happens when the potential energy surface is modulated by changes in the lattice structure? To address this concern in a tractable way, we consider the following scenario: the diffusion of H^+ through a relaxed structure of $(CdSe)_{84}^-$ that is modulated further by its displacement along one of the "breathing" phonon modes as shown in Figure 4.6. Energetic analysis of a "relaxed" system in which the lattice distances have been optimized and augmented by the zero point displacement of a "breathing" phonon mode show that the effect on the lattice expansion and thermalization is to decrease the heights (and to a very small extent, increase the widths) of the internal potential barriers along the diffusion coordinate by as much as ∼50%, relative to the nanocrystals built from the lattice parameters. Therefore, we investigated the effect of uniformly scaling the PES along the internal diffusion coordinate on the quantum mechanical nature of the intercalant (see Figure 4.7).

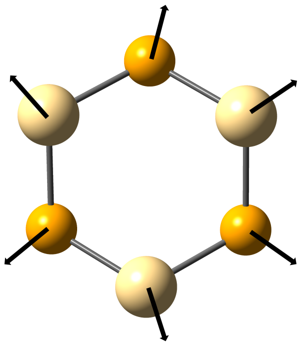

Figure 4.6: Vector displacement representation of a radial breathing mode which would facilitate the lowering of barriers within a QD, only a zoomed in ball and stick representation of the atoms of the intercalating channel is shown for clarity. This particular vibrational mode occurs at a frequency of 60.50 cm^{-1} for $CdSe_{33}^-$.

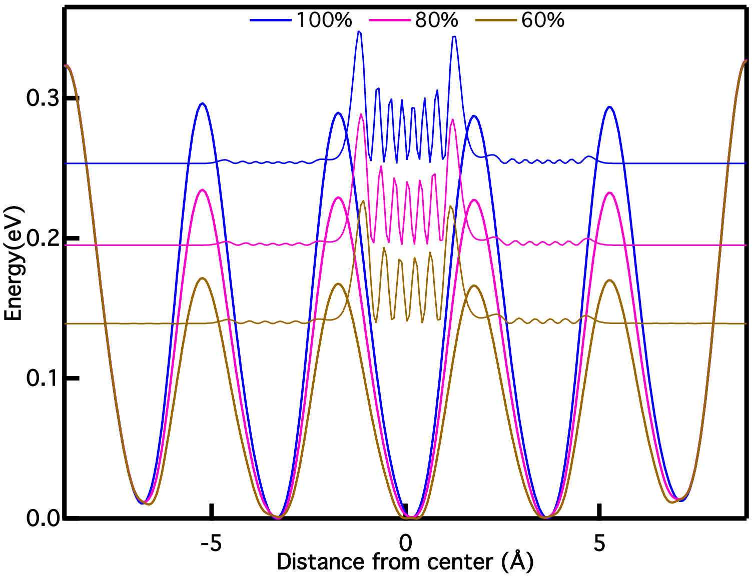

Figure 4.7: Uniformly scaled PBE0/LANL2DZ rigid 1D-PES for the H^+ diffusing along the C_{3v} axis in $(CdSe)_{84}^-$ QD, simulating the effect of the breathing modes that can affect the QD calculations by lowering the inner barriers. The probability distribution of the first diffused state, $|\Psi_{DVR}|^2$, for each is also plotted.

The collective effects of lowered activation barrier on nuclear energy levels are shown in Table 4.4. As the intercalating barrier is lowered, the probability of accessing states at 300 K with significant tunneling diffusion increases somewhat. Figure 4.8 shows the effect of diffusion barrier height on the position uncertainties of H^+ and Li^+ evaluated at 300 K. As the diffusion barrier height decreases, the wave function of H^+ becomes more delocalized, and a stronger quantum influence on the ion diffusion is observed. At the largest scaling, the τ value is ~0.25 for H^+, while for Li^+ in the same material, even upon scaling the internal barriers by 50%, the largest τ observed was ~0.1, indicating mostly classical behavior even under an exaggerated influence of the breathing modes of the QD.

Percentage of original diffusion barrier	Ground State Energy (eV)^a	300K Population (%)^b	Excited State Energy (eV)^a	300K Population (%)^b
100	0.019	17.9	0.253	~0
90	0.017	17.5	0.210	~0
80	0.016	17.1	0.195	~0
70	0.013	16.6	0.130	0.2
60	0.011	16.1	0.117	0.3
50	0.010	15.3	0.104	0.4

Table 4.4: Vibration energy levels for H^+ diffusing along the C_{3v} axis in $\mathbf{(CdSe)_{84}^-}$ QD. The diffusion is affected by the QD breathing mode which allows the inner barriers to be lowered (percentages reflect degree of barrier reduction). Only values corresponding to the ground state (left) and first diffused state (right) are reported for conciseness. ^{a} Energies are given relative to the bottom of the deepest well within the QD. ^{b} Relative population of vibrational levels according to a Boltzmann distribution at T=300K.

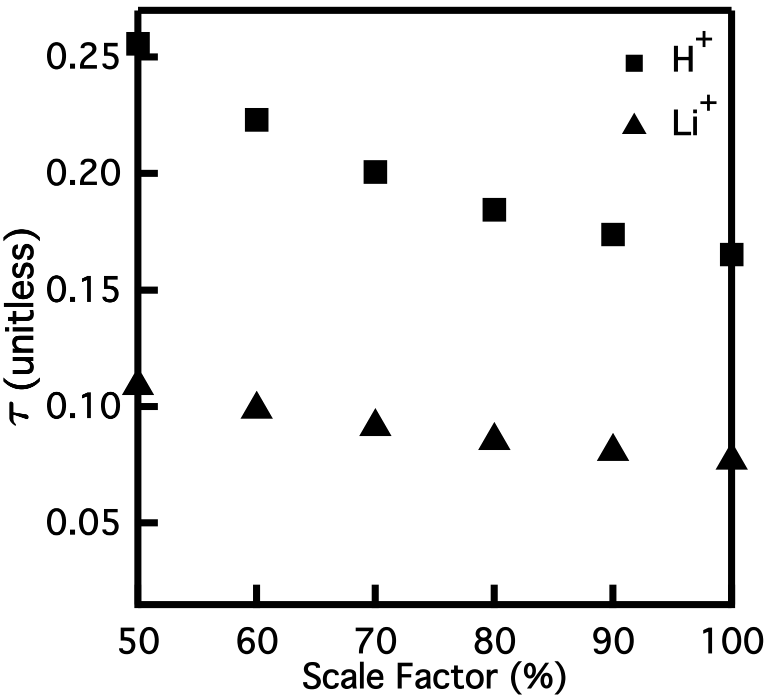

Figure 4.8: Ratios of thermally-averaged position uncertainties for the diffusing ions to the distances between adjacent min/max along the diffusion coordinate, $4\left<\sigma_R\right>/c$, marked as a function of the scaling factor applied to the potential energy surface for the lightest group I cations diffusing along the C_{3v} axis in $(CdSe)_{84}^-$ QD.

4.5 Conclusion

The energetics for ion intercalation along an interstitial channel aligned with the C_{3v} axis of different II-VI binary semiconductor nanocrystals were investigated and the question of whether the dynamics of these intercalants may be described classically, or if the quantum effects are important was also approached from the vantage of the solution to the one-dimensional Schrödinger equations for the diffusing ions using the tools of the discrete variable representation (DVR). A well-calibrated, atomic orbital based electronic structure method was applied to nanoscaled clusters of the semiconductors in order to map out the potential energy surface for light group I cations along a linear interstitial diffusion coordinate. The time-independent nuclear Schrödinger equation was then solved for each intercalating ion and host semiconductor pair, and the results interpreted in light of the uncertainty principle. The density of energy eigenstates for the diffusing ion in the QD can become discrete relative to the thermal energy at room temperature, with increasing splittings in levels and loss of density of bound states resulting from semiconductor hosts with smaller lattice parameters, and intercalating ions of low atomic mass.

Increased internal diffusion barriers are observed in general as the lattice size of nanocrystals decreases.

Analysis of the ratio between the position uncertainty and the distance between adjacent potential minima and maxima suggests that the diffusion of H^+ has significant quantum tunneling characteristics while Na^+ behaves mostly classically. The lattice relaxation is shown to modulate the diffusion PES by lowering the intercalating barrier height by as much as 50%. As a result, the quantum nature of the intercalant is significantly increased.

Recently introduced post-synthetic, diffusion doping procedures are capable of producing much higher dopant concentrations than can be achieved by incorporation of dopants during the nanocrystal growth. The ability to reliably achieve high doping percentages in semiconductor material can have broad-reaching impact for a number of functionalized semiconductor-based devices and technologies. However, not all combinations of host lattices and dopants can be amenable with such a procedure, and oftentimes simple steric arguments alone cannot fully determine the success/failure of a diffusion doping experiment. In this work, we highlight the balance of factors which can determine the compatibility of a given pair of binary semiconductor and intercalant for diffusion doping, ranging from the extent of ionization of the host/lattice species to the effect of lattice relaxation and acoustic phonon modes. We also identify compounds with low internal barriers to diffusion, which can yield faster transport kinetics for diffusion-enabled processes. This is of particular importance to the advancement of lithium ion battery electrode technologies. Future work in this area will perform time-domain simulations (directly in the DVR) to resolve tunneling rates and diffusion constants for the reduced-dimensionality diffusion problem studied herein. Mechanisms for the trapping of different dopants from transient interstitial sites into fixed lattice positions will also be investigated.

Acknowledgment

This work was supported by the National Science Foundation (DMR-1408617). The University of Washington Student Technology Fund is gratefully acknowledged.

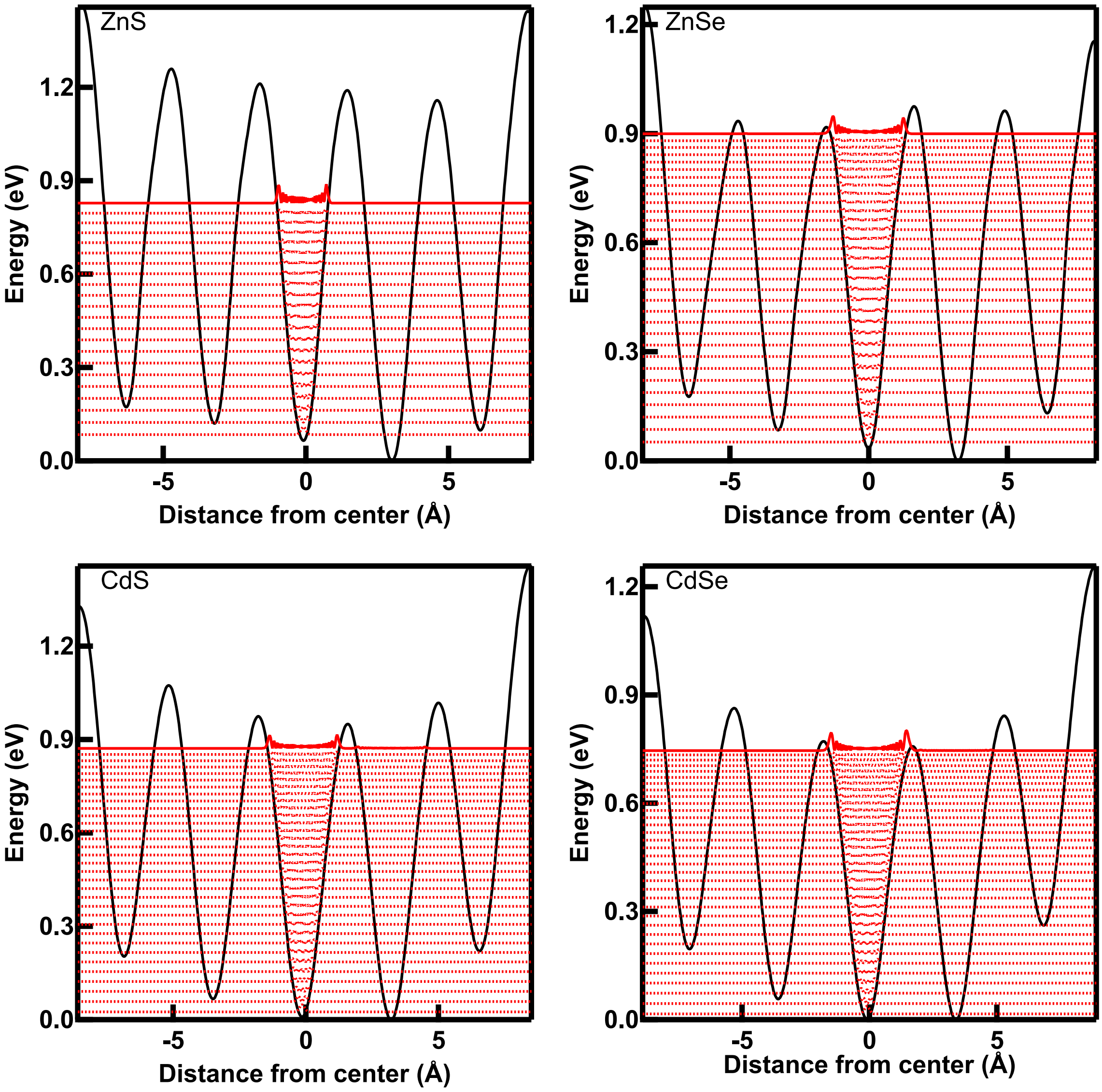

Figure 4.9: Normalized $|\Psi^{i}_{DVR}|^2$ DVR probability distribution functions (dotted red lines, solid red line represents $|\Psi^{i}_{DVR}|^2 \times 2$) for lithium cation in the analyzed reduced QDs. We reported only the ones localized in the central well up to the first diffused state, plotted so that the corresponding base line matches the associated eigenvalue (relative to the 1D-PES, black line). The probability distributions are calculated as the squared values of the corresponding normalized DVR wave functions.

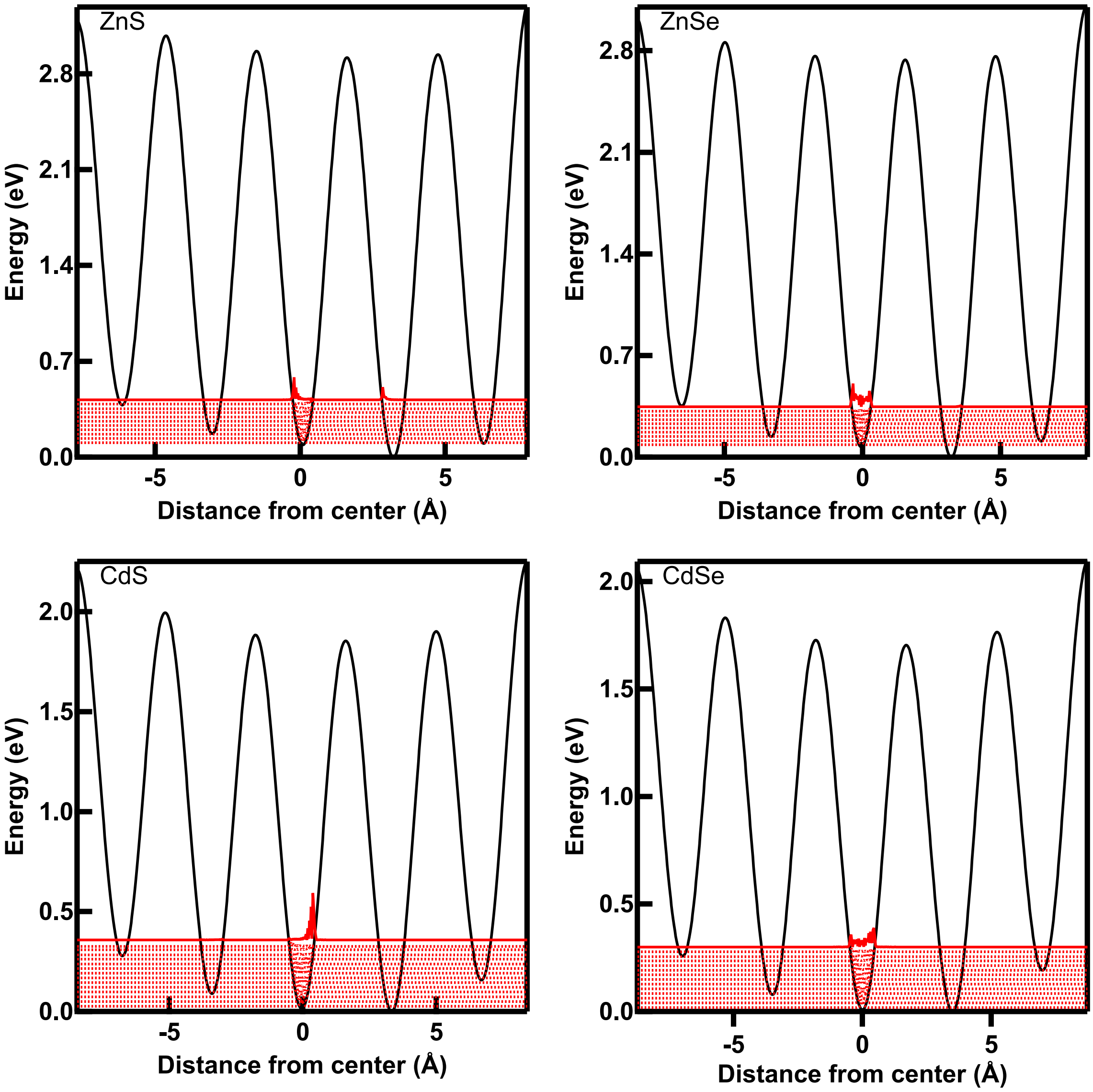

Figure 4.10: Normalized $|\Psi^{i}_{DVR}|^2$ DVR probability distribution functions (dotted red lines, solid red line represents $|\Psi^{i}_{DVR}|^2 \times 2$) for sodium cation in the analyzed reduced QDs. We reported only the ones localized in the central well up to the first diffused state, plotted so that the corresponding base line matches the associated eigenvalue (relative to the 1D-PES, black line). The probability distributions are calculated as the squared values of the corresponding normalized DVR wave functions.

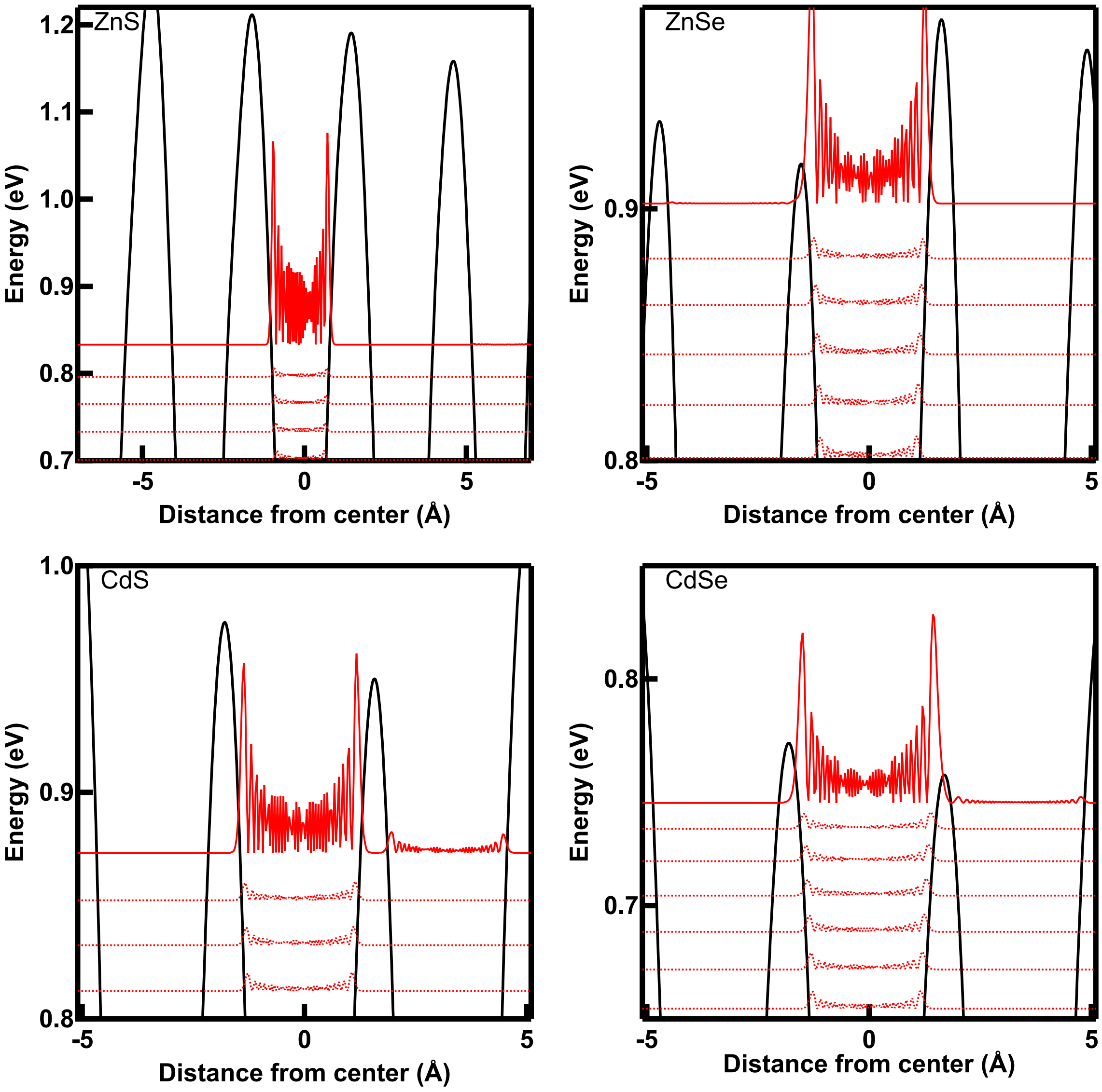

Figure 4.11: Zoomed in images of Figure 4.9.

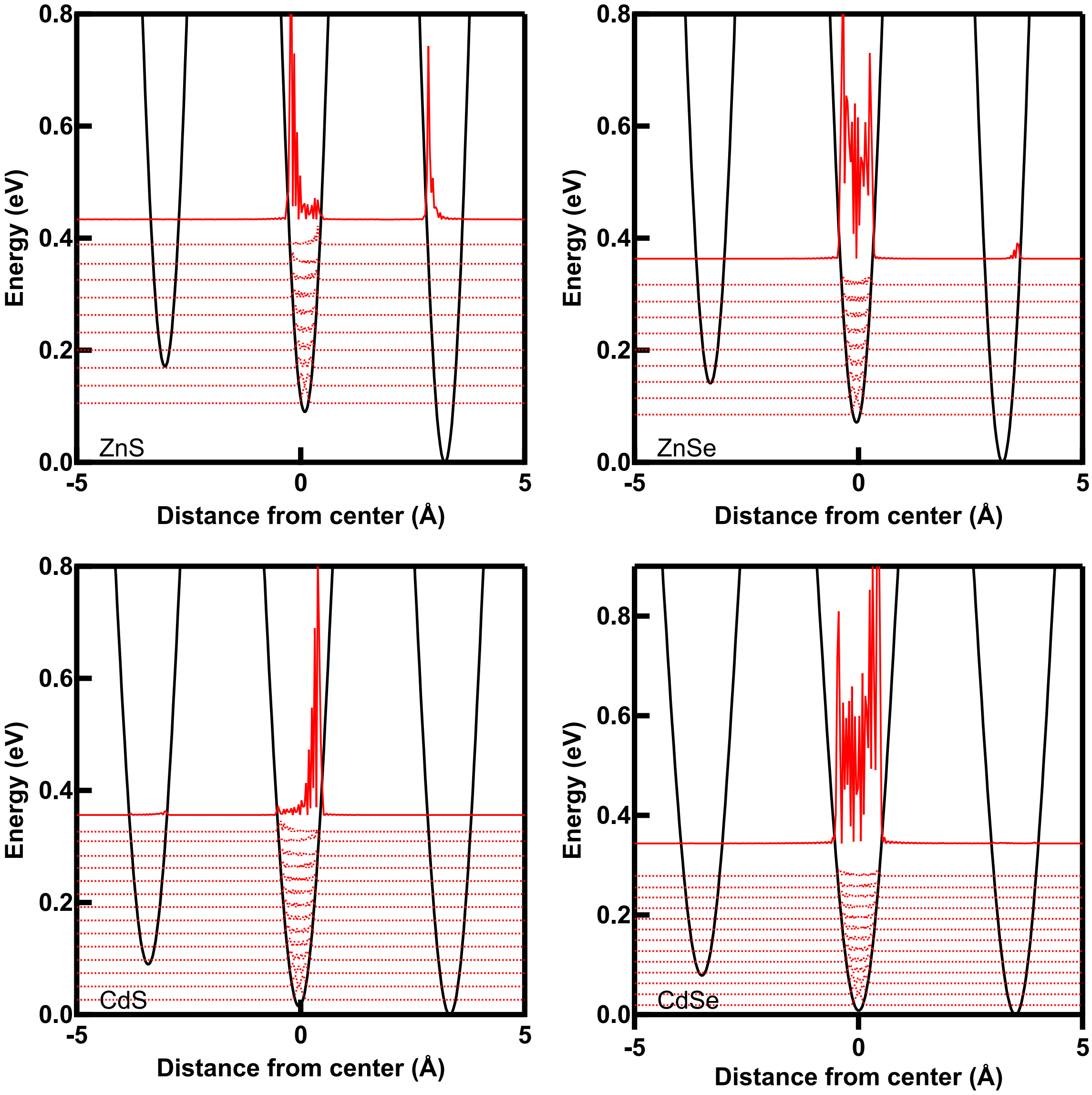

Figure 4.12: Zoomed in images of Figure 4.10.

Bibliography

[1] Ekimov A. I. and Onushchenko A. A. Quantum size effect in three-dimensional microscopic semiconductor crystals. *JETP Lett.*, 34:345–349, 1981.

[2] L. E. Brus. Electron–electron and electron-hole interactions in small semiconductor crystallites: The size dependence of the lowest excited electronic state. *J. Chem. Phys.*, 80(9):4403–4409, 1984.

[3] S. V. Gaponenko. *Optical Properties of Semiconductor Nanocrystals.* Cambridge University Press, 1987.

[4] Konstantatos G., Howard I., Fischer A., Hoogland S., Clifford J., Klem E., Levina L., and Sargent E. H. Ultrasensitive solution-cast quantum dot photodetectors. *Nature*, 442:180–183, 2006.

[5] Caruge J. M., Halpert J. E., Wood V., Bulovic V., and Bawendi M. G. Colloidal quantum-dot light-emitting diodes with metal-oxide charge transport layers. *Nat. Photon.*, 2:247–250, 2008.

[6] Wang Y., Fruhwirth G., Cai E.and Ng T., and Paul R. Selvin. 3d super-resolution imaging with blinking quantum dots. *Nano Lett.*, 13:5233–5241, 2013.

[7] Sargent E. Colloidal quantum dot solar cells. *Nat. Photon.*, 6:133–135, 2012.

[8] Kushima A., Liu X. H., Zhu G., Wang Z. L., Huang J. Y., and Ju Li. Leapfrog cracking and nanoamorphization of zno nanowires during in situ electrochemical lithiation. *Nano Lett.*, 11:4535–4541, 2011.

[9] Remi Beaulac, Lars Schneider, Paul I. Archer, Gerd Bacher, and Daniel R. Gamelin. Light-induced spontaneous magnetization in doped colloidal quantum dots. *Science*, 325(5943):973–976, 2009.

[10] Roest A. L., Houtepen A. J., Kelly J. J., and Vanmaekelbergh D. Electron-conducting quantum-dot solids with ionic charge compensation. *Faraday Discuss.*, 125:55–62, 2004.

[11] Dyson H. J. and Wright P. E. Intrinsically unstructured proteins and their functions. *Nat. Rev. Mol. Cell Biol.*, 6:197–208, 2005.

[12] Dunker A. K., Lawson J. D., Brown C. J., Williams R. M., Romero P., Oh J. S., Oldfield C. J., Campen A. M., Ratliff C. M., Hipps K. W., Ausio J., Nissen M. S., Reeves R., Kang C., Kissinger C. R., Bailey R. W., Griswold M. D., Chiu W., Garner E. C., and Obradovic Z. Intrinsically disordered protein. *J. Mol. Graph. Model.*, 19:26–59, 2001.

[13] Dunker A. K., Obradovic Z., Romero P., Garner E. C., and Brown C. J. Intrinsic protein disorder in complete genomes. *Genome Informormatics*, 11:161–171, 2000.

[14] Ross C. A. and Poirier M. A. What is the role of protein aggregation in neurodegeneration? *Nat. Rev. Mol. Cell. Biol.*, 6:891–898, 2005.

[15] Gardner R. G., Nelson Z. W., and Gottschling D. E. Degradation-mediated protein quality control in the nucleus. *Cell*, 120:734736, 2005.

[16] Oldeld C. J., Cheng Y., Cortese M. S., Romero P., Uversky V. N., and Dunker A. K. Coupled folding and binding with alpha-helix-forming molecular recognition elements. *Biochemistry*, 44:1245412470, 2005.

[17] Fredrickson E. K., Rosenbaum J. C., Locke M. N., Milac T. I., and Gardner R. G. Exposed hydrophobicity is a key determinant for nuclear quality control degradation. *Mol. Bio. Cell.*, 22:23842395, 2011.

[18] Uversky V. N., Oldeld C. J., and Dunker A. K. Intrinsically disordered proteins in human diseases: introducing the d2 concept. *Annu. Rev. Biophys.*, 37:21546, 2008.

[19] Pettersen E. F., Goddard T. D., Huang C. C., Couch G. S., Greenblatt D. M., Meng E. C., and Ferrin T. E. Ucsf chimera – a visualization system for exploratory research and analysis. *J. Comput. Chem.*, 25:1605–1612, 2004.

[20] M. J. Frisch, G. W. Trucks, H. B. Schlegel, G. E. Scuseria, M. A. Robb, J. R. Cheeseman, G. Scalmani, V. Barone, B. Mennucci, G. A. Petersson, H. Nakatsuji, M. Caricato, X. Li, H. P. Hratchian, A. F. Izmaylov, J. Bloino, G. Zheng, J. L. Sonnenberg, M. Hada, M. Ehara, K. Toyota, R. Fukuda, J. Hasegawa, M. Ishida, T. Nakajima, Y. Honda, O. Kitao, H. Nakai, T. Vreven, J. A. Montgomery Jr., J. E. Peralta, F. Ogliaro, M. Bearpark, J. J. Heyd, E. Brothers, K. N. Kudin, V. N. Staroverov, T. Keith, R. Kobayashi, J. Normand, K. Raghavachari, A. Rendell, J. C. Burant, S. S. Iyengar, J. Tomasi, M. Cossi, N. Rega, J. M. Millam, M. Klene, J. E. Knox, J. B. Cross, V. Bakken, C. Adamo, J. Jaramillo, R. Gomperts, R. E. Stratmann, O. Yazyev, A. J. Austin, R. Cammi, C. Pomelli, J. W. Ochterski, R. L. Martin, K. Morokuma, V. G. Zakrzewski, G. A. Voth, P. Salvador, J. J. Dannenberg, S. Dapprich, A. D. Daniels, Ö. Farkas, J. B. Foresman, J. V. Ortiz, J. Cioslowski, and D. J. Fox. Gaussian 09 Revision C.01. Gaussian Inc., Wallingford CT 2010.

[21] Schaftenaar G. and Noordik J.H. Molden: a pre- and post-processing program for molecular and electronic structures. *J. Comput.-Aided Mol. Design*, 14:123–134, 2000.

[22] H. Bentarzi. *Transport in Metal-Oxide-Semiconductor Structures: Mobile Ions Effects on the Oxide Properties*. Engineering Materials. Springer Berlin Heidelberg, 2011.

[23] Moses Ender. An extended homogenized porous electrode model for lithium-ion cell electrodes. *J. Power Sources*, 282:572 – 580, 2015.

[24] Maria L. Sushko, Kevin M. Rosso, Ji-Guang (Jason) Zhang, and Jun Liu. Multiscale simulations of li ion conductivity in solid electrolyte. *J. Phys. Chem. Lett.*, 2(18):2352–2356, 2011.

[25] Bo Song, Junwei Yang, Jijun Zhao, and Haiping Fang. Intercalation and diffusion of lithium ions in a carbon nanotube bundle by *ab Initio* molecular dynamics simulations. *Energy Environ. Sci.*, 4:1379–1384, 2011.

[26] Marc Doyle, Thomas F. Fuller, and John Newman. Modeling of galvanostatic charge and discharge of the lithium/polymer/insertion cell. *J. Electrochem. Soc.*, 140(6):1526–1533, 1993.

[27] Sbastien Sailler, Jonathan Deseure, Olivier Doche, and Yann Bultel. First 3d-modeling of proton-conducting sofc's interconnect. *ECS Trans.*, 35(1):2571–2579, 2011.

[28] Carolyn N. Valdez, Alina M. Schimpf, Daniel R. Gamelin, and James M. Mayer. Proton-controlled reduction of zno nanocrystals: Effects of molecular reductants, cations, and thermodynamic limitations. *J. Am. Chem. Soc.*, 138(4):1377–1385, 2016.

[29] Miles N. Braten, Daniel R. Gamelin, and James M. Mayer. Reaction dynamics of proton-coupled electron transfer from reduced zno nanocrystals. *ACS Nano*, 9(10):10258–10267, 2015.

[30] Alina M. Schimpf, Kathryn E. Knowles, Gerard M. Carroll, and Daniel R. Gamelin. Electronic doping and redox-potential tuning in colloidal semiconductor nanocrystals. *Acc. Chem. Res.*, 48(7):1929–1937, 2015.

[31] Peter G Bruce, Bruno Scrosati, and Jean-Marie Tarascon. Nanomaterials for rechargeable lithium batteries. *Angew. Chem.*, 47(16):2930–2946, 2008.

[32] N Balke, S Jesse, AN Morozovska, E Eliseev, DW Chung, Y Kim, L Adamczyk, RE Garcia, N Dudney, and SV Kalinin. Nanoscale mapping of ion diffusion in a lithium-ion battery cathode. *Nat. Nano.*, 5(10):749–754, 2010.

[33] Norio Miura, Motoaki Iio, Geyu Lu, and Noboru Yamazoe. Solid-state amperometric no_2 sensor using a sodium ion conductor. *Sensor Actuat. B-Chem.*, 35(1):124–129, 1996.

[34] R. Hanson, L. H. Willems van Beveren, I. T. Vink, J. M. Elzerman, W. J. M. Naber, F. H. L. Koppens, L. P. Kouwenhoven, and L. M. K. Vandersypen. Single-shot readout of electron spin states in a quantum dot using spin-dependent tunnel rates. *Phys. Rev. Lett.*, 94:196802, May 2005.

[35] P. Michler, A. Kiraz, C. Becher, W. V. Schoenfeld, P. M. Petroff, Lidong Zhang, E. Hu, and A. Imamoglu. A quantum dot single-photon turnstile device. *Science*, 290(5500):2282–2285, 2000.

[36] David Mocatta, Guy Cohen, Jonathan Schattner, Oded Millo, Eran Rabani, and Uri Banin. Heavily doped semiconductor nanocrystal quantum dots. *Science*, 332(6025):77–81, 2011.

[37] Tadashi Watanabe, Akira Fujishima, Osamu Tatsuoki, and Ken-ichi Honda. ph-dependence of spectral sensitization at semiconductor electrodes. *Bull. Chem. Soc. Jpn.*, 49(1):8–11, 1976.

[38] U M Gosele. Fast diffusion in semiconductors. *Ann. Rev. Mater. Sci.*, 18(1):257–282, 1988.

[39] Derek Shaw. *Springer Handbook of Electronic and Photonic Materials*, chapter Diffusion in Semiconductors, pages 121–135. Springer US, Boston, MA, 2007.

[40] G.E. Murch and A.S. Nowick. *Diffusion in Crystalline Solids*. Materials science and technology. Academic Press, 1984.

[41] Petr Krtil, Ladislav Kavan, and Dina Fattakhova. Insertion of lithium into mesoscopic anatase electrodes – an electrochemical and *in-situ* eqcm study. *J. Solid State Electrochem.*, 1(1):83–87, 1997.

[42] L. Andrew Lyon and Joseph T. Hupp. Energetics of semiconductor electrode/solution interfaces: Eqcm evidence for charge-compensating cation adsorption and intercalation during accumulation layer formation in the titanium dioxide/acetonitrile system. *J. Phys. Chem.*, 99(43):15718–15720, 1995.

[43] MG Wardle, JP Goss, and PR Briddon. First-principles study of the diffusion of hydrogen in zno. *Phys. Rev. Lett.*, 96(20):205504, 2006.

[44] Yu Sun, Sheng-Yi Xie, and Xing Meng. A first-principles study on hydrogen in zns: Structure, stability and diffusion. *Phys. Lett. A*, 379(5):487–490, 2015.

[45] J-M Tarascon and Michel Armand. Issues and challenges facing rechargeable lithium batteries. *Nature*, 414(6861):359–367, 2001.

[46] PR Bueno and ER Leite. Nanostructured li ion insertion electrodes. 1. discussion on fast transport and short path for ion diffusion. *J. Phys. Chem. B*, 107(34):8868–8877, 2003.

[47] Vladimir A. Vlaskin, Charles J. Barrows, Christian S. Erickson, and Daniel R. Gamelin. Nanocrystal diffusion doping. *J. Am. Chem. Soc.*, 135(38):14380–14389, 2013. PMID: 24028655.

[48] Charles J. Barrows, Pradip Chakraborty, Lindsey M. Kornowske, and Daniel R. Gamelin. Tuning equilibrium compositions in colloidal $cd_{1x}mn_x$se nanocrystals using diffusion doping and cation exchange. *ACS Nano*, 10(1):910–918, 2016.

[49] Sebastian Polarz, A Orlov, Axel Hoffmann, MR Wagner, C Rauch, Rudolf Kirste, Wolfgang Gehlhoff, Yilmaz Aksu, Matthias Driess, Maurits WE Van den Berg, and M Lehmann. A systematic study on zinc oxide materials containing group i metals (li, na, k)- synthesis from organometallic precursors, characterization, and properties. *Chem. Mater.*, 21(16):3889–3897, 2009.

[50] M. G. Bawendi, M. L. Steigerwald, and L. E. Brus. The quantum mechanics of larger semiconductor clusters (" quantum dots"). *Annu. Rev. Phys. Chem.*, 41(1):477–496, 1990.

[51] A. Rogach. *Semiconductor Nanocrystal Quantum Dots: Synthesis, Assembly, Spectroscopy and Applications*. Springer ebook collection / Chemistry and Materials Science 2005-2008. Springer Vienna, 2008.

[52] Mudit Dixit, Hamutal Engel, Reuven Eitan, Doron Aurbach, Mikhael D. Levi, Monica Kosa, and Dan Thomas Major. Classical and quantum modeling of li and na diffusion in fepo4. *J. Phys. Chem. C*, 119(28):15801–15809, 2015.

[53] M. J. Frisch, G. W. Trucks, H. B. Schlegel, G. E. Scuseria, M. A. Robb, J. R. Cheeseman, G. Scalmani, V. Barone, B. Mennucci, G. A. Petersson, H. Nakatsuji, M. Caricato, X. Li, H. P. Hratchian, A. F. Izmaylov, J. Bloino, G. Zheng, J. L. Sonnenberg, W. Liang, M. Hada, M. Ehara, K. Toyota, R. Fukuda, J. Hasegawa, M. Ishida, T. Nakajima, Y. Honda, O. Kitao, H. Nakai, T. Vreven, Jr. J. A. Montgomery, J. E. Peralta, F. Ogliaro, M. Bearpark, J. J. Heyd, E. Brothers, K. N. Kudin, V. N. Staroverov, T. Keith, R. Kobayashi, J. Normand, K. Raghavachari, A. Rendell, J. C. Burant, S. S. Iyengar, J. Tomasi, M. Cossi, N. Rega, J. M. Millam, M. Klene, J. E. Knox, J. B. Cross, V. Bakken, C. Adamo, J. Jaramillo, R. Gomperts, R. E. Stratmann, O. Yazyev, A. J. Austin, R. Cammi, C. Pomelli, J. W. Ochterski, R. L. Martin, K. Morokuma, V. G. Zakrzewski, G. A. Voth, P. Salvador, J. J. Dannenberg, S. Dapprich, P. V. Parandekar, N. J. Mayhall, A. D. Daniels, Ö. Farkas, J. B. Foresman, J. V. Ortiz, J. Cioslowski, and D. J. Fox. Gaussian Development Version Revision H.12+. Gaussian Inc., Wallingford CT 2011.

[54] Ekateriana Badaeva, Yong Feng, Daniel R. Gamelin, and Xiaosong Li. Investigation of pure and co^{2+}-doped zno quantum dot electronic structures using the density functional theory: Choosing the right functional. *New J. Phys.*, 10:055013, 2008.

[55] Ekateriana Badaeva, Christine M. Isborn, Yong Feng, Stefan T. Ochsenbein, Daniel R. Gamelin, and Xiaosog Li. Theoretical characterization of electronic transitions in co^{2+}- and mn^{2+}-doped zno nanocrystals. *J. Phys. Chem. C*, 113(20):8710–8717, 2009.

[56] R. T. Downs and M. Hall-Wallace. The american mineralogist crystal structure database. *Amm. Mineral.*, 88(1):247–250, 2003.

[57] Carlo Adamo and Vincenzo Barone. Toward reliable density functional methods without adjustable parameters: The pbe0 model. *J. Chem. Phys.*, 110:6158, 1999.

[58] J. P. Perdew, K. Burke, and M. Ernzerhof. Generalized gradient approximation made simple. *Phys. Rev. Lett.*, 77(18):3865–3868, 1996.

[59] J. P. Perdew, K. Burke, and M. Ernzerhof. Generalized gradient approximation made simple [phys. rev. lett. 77, 3865 (1996)]. *Phys. Rev. Lett.*, 78:1396–1396, Feb 1997.

[60] T. H. Dunning Jr and P. J. Hay. *Methods of electronic structure theory.* Ed. H. F. Schaefer III, Vol 3, Springer, 1977.

[61] W. R. Wadt and P. J. Hay. Ab initio effective core potentials for molecular calculations. potentials for main group elements na to bi. *J. Chem. Phys.*, 82(1):284–298, 1985.

[62] P. J. Hay and W. R. Wadt. Ab initio effective core potentials for molecular calculations. potentials for the transition metal atoms sc to hg. *J. Chem. Phys.*, 82(1):270–283, 1985.

[63] Thom H. Dunning. Gaussian basis sets for use in correlated molecular calculations. i. the atoms boron through neon and hydrogen. *J. Chem. Phys.*, 90(2):1007–1023, 1989.

[64] Rémi Beaulac, Yong Feng, Joseph W. May, Ekaterina Badaeva, Daniel R. Gamelin, and Xiaosong Li. Orbital pathways for mn^{2+}-carrier *sp*–*d* exchange in diluted magnetic semiconductor quantum dots. *Phys. Rev. B*, 84:195324, 2011.

[65] Joseph W. May, Ryan J. McMorris, and Xiaosong Li. Ferromagnetism in *p*-type manganese-doped zinc oxide quantum dots. *J. Phys. Chem. Lett.*, 3:1374–1380, 2012.

[66] Joseph W May, Jiao Ma, Ekaterina Badaeva, and Xiaosong Li. Effect of excited-state structural relaxation on midgap excitations in co2+-doped zno quantum dots. *J. Phys. Chem. C*, 118(24):13152–13156, 2014.

[67] J. J. Goings, A. M. Schimpf, J. W. May, R. W. Johns, D. R. Gamelin, and X. Li. Theoretical characterization of conduction-band electrons in photodoped and aluminum-doped zinc oxide (azo) quantum dots. *J. Phys. Chem. C*, 118(46):26584–26590, 2014.

[68] Bo Peng, Joseph W. May, Daniel R. Gamelin, and Xiaosong Li. Effects of crystallographic and shape anisotropies on dopant-carrier exchange interactions in magnetic semiconductor quantum dots. *J. Phys. Chem. C*, 118:7630–7636, 2014.

[69] Liam R. Bradshaw, Joseph W. May, Jillian L. Dempsey, Xiaosong Li, and Daniel R. Gamelin. Ferromagnetic excited-state mn^{2+} dimers in zn$_{1-x}$mn$_x$se quantum dots observed by time-resolved magnetophotoluminescence. *Phys. Rev. B*, 89:115312, 2014.

[70] J. C. Light, I. P. Hamilton, and J. V. Lill. Generalized discrete variable approximation in quantum mechanics. *J. Chem. Phys.*, 82(3):1400–1409, 1985.

[71] D. T. Colbert and W. H. Miller. A novel discrete variable representation for quantum mechanical reactive scattering via the s-matrix kohn method. *J. Chem. Phys.*, 96(3):1982–1991, 1992.

[72] J. C. Light and T. Carrington Jr. Discrete-variable representations and their utilization. *Adv. Chem. Phys.*, 114:263–310, 2000.

[73] D. Tannor. *Introduction to quantum mechanics*. University Science Books, 2007.

[74] R. Gelabert, M. Moreno, J. M. Lluch, and A. Lledós. Elongated dihydrogen complexes: A combined electronic dft+ nuclear dynamics study of the [ru (h h)(c5h5)(h2pch2ph2)]+ complex. *J. Am. Chem. Soc.*, 119(41):9840–9847, 1997.

[75] C. Scheurer, R. Wiedenbruch, R. Meyer, R.R. Ernst, and D.M. Heinekey. Quantum mechanical exchange in a transition metal hydride complex: Nmr data for [cp (pph3) irh3]+ fitted by a two-dimensional model. *J. Chem. Phys.*, 106(1):1–10, 1997.

[76] R. Gelabert, M. Moreno, J. M. Lluch, and A. Lledós. *J. Am. Chem. Soc.*, 120(32):8168–8176, 1998.

[77] L. Torres, R. Gelabert, M. Moreno, and J. M. Lluch. Nuclear dynamics discrete variable representation study of the equilibrium isotope effect on h2 binding in m (η 2-h2) l n complexes: An effective theoretical way to account for anharmonicity. *J. Phys. Chem. A*, 104(33):7898–7905, 2000.

[78] BP Singh, VS Baghel, and KS Baghel. Electronegativity, fractional ionic character and refractive index of binary compounds. *Indian J. Pure Appl. Phys.*, 47(11):793, 2009.

[79] BP Singh, AK Ojha, and S Tripti. Analysis of ionicity parameters and photoelastic behaviour of a n b 8–n type crystals. *Physica B*, 350(4):338–347, 2004.

List of Figures

List of Tables